



# CMB Cold Spot in the Planck Light

M. Farhang and S. M. S. Movahed

Department of Physics, Shahid Beheshti University, 1983969411, Tehran, Iran; [m\\_farhang@sbu.ac.ir](mailto:m_farhang@sbu.ac.ir)

Received 2019 December 16; revised 2020 October 27; accepted 2020 November 6; published 2021 January 5

## Abstract

The Cold Spot, with an unusually cold region surrounded by a hot ring, is a statistically significant anomaly in the cosmic microwave background (CMB) sky. In this work we assess whether different sets of multiple subvoids based on the 2dF-VST ATLAS Cold Spot galaxy redshift survey or a collapsing cosmic texture could have produced such an anomaly through a simultaneous search for their gravitational redshift and lensing signatures on the Planck CMB temperature anisotropies. We use patches with radii  $R = 10^\circ$  and  $R = 20^\circ$  to account for the inner cold region as well as the outer hot ring. As the void model, we explore two sets of  $\Lambda$ LTB templates characterized by different values of the model's free parameters, and a top-hat void template. We detect higher than expected gravitational redshift amplitudes for the first two sets,  $\mathcal{A}_{rs} = 5.4 \pm 1.4$  and  $\mathcal{A}_{rs} = 14.4 \pm 3.8$ , and lower than expected for the top-hat model,  $\mathcal{A}_{rs} = 0.3 \pm 0.1$ . The amplitudes for the lensing imprint are consistent with zero for all these subvoid models. The estimated amplitude for the texture imprint from the gravitational redshift measurement implies the energy scale of the texture, parameterized by  $\epsilon$ , to be  $\epsilon = (7.6 \pm 2.0) \times 10^{-5}$ , with no detection of the lensing trace. We note that the deviation of the subvoid amplitudes from unity and the inability of the texture and some of the void profiles to reproduce the hot ring indicate theoretical insufficiencies, either in the construction of the model or in the assumed gravitational and cosmological framework leading to the imprints for the structures.

*Unified Astronomy Thesaurus concepts:* [Cosmic microwave background radiation \(322\)](#); [Astronomy data acquisition \(1860\)](#); [Observational cosmology \(1146\)](#); [Cosmology \(343\)](#); [Astronomy data analysis \(1858\)](#)

## 1. Introduction

The Cold Spot (CS) in the cosmic microwave background (CMB) map is an unusually cold and large region, located at  $(l, b) \sim (208^\circ, -57^\circ)$  with the mean temperature decrement  $\Delta T \approx -150 \mu\text{K}$  in a  $5^\circ$  radius, and is among the robust large-scale CMB anomalies. It was first detected in the WMAP data through the Gaussianity test of CMB anisotropies using Spherical Mexican Hat Wavelets with  $\approx(2 \sim 3) \sigma$  significance (Vielva et al. 2004) and its significance and properties were further explored through other techniques (Larson & Wandelt 2004; Cruz et al. 2005, 2006, 2007; Vielva 2010). The existence and anomalous nature of the CS in the  $\Lambda$ CDM model was subsequently confirmed by Planck observations (Planck Collaboration et al. 2014, 2016). Although originally detected due to its unusual coldness, it is argued that the anomalous nature of the CS is in fact due to its peculiar template of a central cold region surrounded by a hot ring, subtending to the radius of  $R \sim 15^\circ$  (Zhang & Huterer 2010; Nadathur et al. 2014; Kovács 2018).

The chances that Gaussian and isotropic initial conditions, as predicted by standard inflationary scenarios (see, e.g., Liddle & Lyth 2000), have led to such a large and relatively cold region are low, at the 0.5% level (Cruz et al. 2005, 2006, 2007). See Zhang & Huterer (2010) for a different viewpoint. The roles of systematics and foreground contamination are shown to be negligible in producing the CS (Cruz et al. 2005, 2006). Therefore there have been speculations of the CS being produced by secondary sources of anisotropy such as a supervoid or a cosmic texture. Inoue & Silk (2006, 2007) showed that a huge underdense region with density contrast  $\delta_V \sim -0.3$  and comoving radius  $R_V \sim 200\text{--}300 \text{ Mpc}/h$  located at  $z_V \approx 1$  could lead to such a pattern of anisotropy. A completely empty void, i.e., with  $\delta_V \sim -1$ , would require a smaller radius  $R_V \sim 120 \text{ Mpc}/h$  to agree with observations (Rudnick et al. 2007). However,  $\Lambda$ CDM-based simulations suggest

typical void sizes of  $R_V \sim 10 \text{ Mpc}/h$  (with  $\delta_V \sim -0.8$ ), rendering such huge voids unlikely to be found (Hoyle & Vogeley 2004; Colberg et al. 2005; Patiri et al. 2006; Platen et al. 2008; Mackenzie et al. 2017). Also a lack of high redshift anomalies in the redshift distribution of galaxies rules out the existence of a high redshift supervoid in the direction of the CS anomaly (Hoyle & Vogeley 2004; Patiri et al. 2006; Bremer et al. 2010; Granett et al. 2010; Smith & Huterer 2010; Mackenzie et al. 2017).

On the other hand, there is growing observational evidence supporting the existence of a shallow but large supervoid at low redshift, in the constellation Eridanus, aligned with the CS line of sight (Rudnick et al. 2007; Bremer et al. 2010; Granett et al. 2010; Smith & Huterer 2010; Szapudi et al. 2015). Galaxy catalogs are consistent with a large supervoid with radius  $R_V = 220 \pm 50 \text{ Mpc}/h$ , and underdensity  $\delta_V = -0.14 \pm 0.04$  centered at  $z_V = 0.22 \pm 0.03$  (Szapudi et al. 2015; Kovács & García-Bellido 2016; Courtois et al. 2017). However, the actual shape of this rare matter fluctuation is not fully clear yet (Kovács & García-Bellido 2016; Mackenzie et al. 2017). The secondary CMB temperature decrement due to such a supervoid is estimated to be  $\sim 20 \mu\text{K}$ , much smaller than the observed CS temperature, and the predicted angular profile of CMB temperature anisotropy generated by certain models of supervoids in the  $\Lambda$ CDM cosmology differs from the observed CMB cold spot (Nadathur et al. 2014; Zibin 2014; Szapudi et al. 2015; Finelli et al. 2016; Marcos-Caballero et al. 2016). Mackenzie et al. (2017) explored the substructure of the CS region in the 2dF-VST ATLAS Cold Spot galaxy redshift survey and reported four subvoids in the redshift range of 0.14–0.42. They also concluded that the sum of the induced anisotropies by these voids is too low to explain the observed CMB CS.

However, recent studies have claimed that there is probably a factor of 5–10 mismatch between the simulation-based and observed temperature decrements from various supervoids

(Kovács 2018). This excess signal offers a challenging opportunity for exploring beyond  $\Lambda$ CDM theories (e.g., Rudnick et al. 2007; Papai & Szapudi 2010; Papai et al. 2011; Flender et al. 2013; Hotchkiss et al. 2014). It has been argued that supervoids could lead to an enhanced signature in cosmological models other than  $\Lambda$ CDM (see, e.g., Beck et al. 2018). For other noncosmological suggestions as possible ways out of this mismatch, see Flender et al. (2013) and Kovács & Granett (2015).

An alternative to voids, first proposed by Cruz et al. (2007), is a collapsing cosmic texture. Collapsing textures could cause a CS on the CMB sky through gravitational interaction with the photons passing nearby. We here note that there is an argument in the literature against collapsing cosmic textures as viable sources of the CS anomaly. Feeney et al. (2011) use a hierarchical Bayesian analysis to search for the texture model in WMAP7 data where selection biases are automatically accounted for. They found no statistical preference for the texture model compared to the standard model with no textures (see also Peiris 2014). Further independent probes in the search of collapsing cosmic textures are necessary to assess the reality of their existence. Textures could lens the CMB E-mode anisotropies and turn them partially to B-mode. This B-mode signal could serve as a texture probe (García-Bellido et al. 2011). Lensing by texture would also leave an imprint on the 21 cm signal, if given a long dedicated observation time (Kovetz & Kamionkowski 2013). In spite of the above arguments against textures, we still include a collapsing texture among the candidates for the CS origin. Given the importance of the Planck data set and the history of the study of the texture as a candidate, we find it worthwhile to see what Planck has to say about it, irrespective of, and unbiased by, other data sets, simply as a candidate along with more viable candidates.

More specifically, CMB photons passing through or nearby these structures, on their way to reach us, experience gravitational redshift and lensing. We simultaneously measure, for the first time, the amplitudes of these two imprints for voids and a cosmic texture as observed by Planck and assess their consistency. If consistent, these measurements would imply the viability of the assumptions made in the template construction. Their inconsistency, on the other hand, may call for a different parameterization of the templates or different parameter values, or even more severely, challenge the role of these structures in generating the CS.

The rest of this paper is organized as follows. In Section 2 we introduce two sets of well-motivated candidates, voids and a collapsing cosmic texture, as possible sources of the CS and discuss their gravitational redshift and lensing imprints on the temperature of CMB photons. The mathematical framework for the analysis of these imprints is explained in Section 3, and the results are presented in Section 4. We conclude in Section 5. Whenever needed, the standard  $\Lambda$ CDM cosmology, consistent with the Planck 2018 data (Planck Collaboration et al. 2020a), is assumed throughout.

## 2. Candidates

In this section we introduce two sets of physically motivated candidates as possible origins of the CMB CS, i.e., voids in Section 2.1 and a collapsing cosmic texture in Section 2.2. We discuss the gravitational redshift and lensing of CMB photons as they pass through or close to these intervening structures.

### 2.1. Multiple Subvoids

An expanding local void can produce gravitational redshift and thus temperature decrements in CMB photons passing through it, through the combination of the linear Integrated Sachs–Wolfe (ISW; Sachs & Wolfe 1967) and the nonlinear Rees–Sciama effects (Rees & Sciama 1968). The linear effect is shown to substantially dominate the second-order nonlinear contribution (Cai et al. 2010; Nadathur et al. 2014). The nonlinear effect is not therefore considered here. This ISW imprint is sensitive to the expansion history of the universe at late times and is therefore considered as a probe of dark energy (Peebles 1984; Hu & White 1996; Afshordi 2004; Acquaviva & Baccigalupi 2006; Amendola et al. 2008; Schäfer 2008; Carbone et al. 2013; Ade et al. 2016; Mostaghel et al. 2018).

In this section, we introduce two sets of void models. In Section 2.1.1 we use as our void templates the multiple subvoids reported by Mackenzie et al. (2017) found through mapping the Cold Spot region. These voids are modeled as (basic and modified) ALTB spherical underdensities (Finelli et al. 2016). For reasons to be discussed, we also use a different void profile in Section 2.1.2, described by a sharply compensated top-hat radial template (Martínez-González et al. 1990; Martínez-González & Sanz 1990; Cruz et al. 2008).

#### 2.1.1. ALTB Subvoids

The substructure of the core of the CMB cold spot has been recently explored based on the 2dF-VST ATLAS Cold Spot galaxy redshift survey (Mackenzie et al. 2017). They reported voids at four redshifts with various sizes and underdensities. We use these subvoids as our main set of void candidates and explore whether the CMB CS could be interpreted as the combined ISW imprints of these voids.

We follow the void underdensity template used in Mackenzie et al. (2017). It was originally proposed by Finelli et al. (2016) in the context of CS as an underdensity in the ALTB metric (García-Bellido & Haugboelle 2008)

$$ds^2 = -dt^2 + \frac{A'(r, t)^2}{1 - k(r)} dr^2 + A(r, t)^2 d\Omega^2 \quad (1)$$

with the following spatial curvature

$$k(r) = k_0 r^2 \exp\left(-\frac{r^2}{R_V^2}\right), \quad (2)$$

where  $R_V$  is the radius of the spherically symmetric underdensity. With the FRW metric,  $A(r, t) = a(t)r$  where  $a(t)$  is a scale factor. This void model is shown to be well approximated by a linear potential perturbation  $\Phi$  in a flat FRW background, where

$$\Phi(\tau, r) = \Phi_0 \exp\left(-\frac{r^2}{R_V^2}\right) {}_2F_1\left[1, \frac{1}{3}, \frac{11}{6}, \frac{-\Omega_\Lambda}{\Omega_m(1+z)^3}\right]. \quad (3)$$

Here  ${}_2F_1$  is a hypergeometric function and  $\tau$  is the conformal time in the FRW metric. One can use the Poisson equation to get the density profile for the potential of Equation (3)

$$\delta(r, z_V) = \delta_V g(z_V) \left(1 - \frac{2}{3} \frac{r^2}{R_V^2}\right) \exp\left(-\frac{r^2}{R_V^2}\right), \quad (4)$$

where  $\delta_V$  and  $z_V$  are the void underdensity and redshift. Also  $r$  is the distance from the void center and  $g(z)$  is the growth factor

**Table 1**

Characteristics of the Subvoid Candidates Considered in Section 2.1, Described by the Triplets  $(R_V, z_V, \delta_V)$  Representing the Comoving Radius, Redshift, and Underdensity of the Subvoids, Respectively

	Subvoid 1	Subvoid 2	Subvoid 3	Subvoid 4
$R_V$ (Mpc/h)	119	50	59	168
$z_V$	0.14	0.26	0.30	0.42
$\delta_V$	-0.34	-0.87	-1.00	-0.62

**Note.** The values are taken from Table 3 of Mackenzie et al. (2017).

at redshift  $z$ . We also have

$$\Phi_0 = \frac{\Omega_m}{4} \frac{H_0^2 R_V^2 \delta_V}{{}_2F_1\left[1, \frac{1}{3}, \frac{11}{6}, \frac{-\Omega_\Lambda}{\Omega_m}\right]}. \quad (5)$$

The induced ISW temperature anisotropies in CMB photons by this density contrast would be

$$\begin{aligned} \delta T_{rs}(\theta) \approx & \frac{3\sqrt{\pi}}{22} \delta_V \frac{H(z_V) \Omega_\Lambda {}_2F_1\left[2, \frac{4}{3}, \frac{17}{6}, \frac{-\Omega_\Lambda}{\Omega_m(1+z_V)^3}\right]}{H_0(1+z_V)^4 {}_2F_1\left[1, \frac{1}{3}, \frac{11}{6}, \frac{-\Omega_\Lambda}{\Omega_m}\right]} \\ & \times (H_0 R_V/c)^3 \left(1 + \operatorname{erf}\left[\frac{c z_V}{H(z_V) R_V}\right]\right) \exp\left(-\frac{\theta^2}{\theta_V^2}\right) \end{aligned} \quad (6)$$

where  $\delta T \equiv \Delta T/T_{\text{CMB}}$  and the subscript rs labels the redshifted signal. We stress that the main assumption in this model is the Gaussian profile of the spatial curvature in Equation (2). The induced anisotropy is shown to be equivalent whether calculated in an exact  $\Lambda$ TBM framework or approximated as a perturbation in an FRW universe (Nadathur et al. 2014).

Besides the gravitational redshift, photons that pass through the void also experience gravitational lensing. The lensed temperature field,  $\delta \tilde{T}$ , for small radial deflection angle is expressed as

$$\delta \tilde{T}(\theta) = \delta T(\theta + \alpha(\theta)) \simeq \delta T(\theta) + \delta T_{\text{ln}}(\theta), \quad (7)$$

where  $\delta T$  is the unlensed map,  $\delta T_{\text{ln}} \equiv \alpha(\theta) \partial \delta T(\theta) / \partial \theta$ , and  $\alpha(\theta)$  is the template for the lensing deflection angle. The subscript ln labels the gravitational lensing effect. The deflection angle induced by the void of Equation (4) is given by

$$\begin{aligned} \alpha(\theta) \approx & -\delta_V \frac{D_{\text{LS}} D_{\text{L}}}{D_{\text{S}}} \frac{2 R_V H_0^2}{c^2} \frac{\Omega_m}{{}_2F_1\left[1, \frac{1}{3}, \frac{11}{6}, \frac{-\Omega_\Lambda}{\Omega_m}\right]} \\ & \times {}_2F_1\left[1, \frac{1}{3}, \frac{11}{6}, \frac{-\Omega_\Lambda}{\Omega_m(1+z_V)^3}\right] \theta \exp\left(-\frac{\theta^2}{\theta_V^2}\right). \end{aligned} \quad (8)$$

where  $D_{\text{L}}$  and  $D_{\text{S}}$  are the observer's comoving distances to the lens (here, the center of the void) and the source (here, the last scattering surface), and  $D_{\text{LS}}$  represents the source distance to the lens. Table 1 presents the subvoid characteristics as used in this work, based on Table 3 of Mackenzie et al. (2017), and Figure 1 illustrates the corresponding radial profiles for the induced ISW anisotropies (up) and the lensing deflection angle (bottom). We refer to these basic  $\Lambda$ TB subvoids as  $V_1$ – $V_4$ . It is evident from the figure and also expected from Equation (6) that the  $\Lambda$ TB voids cannot produce hot rings, or even more

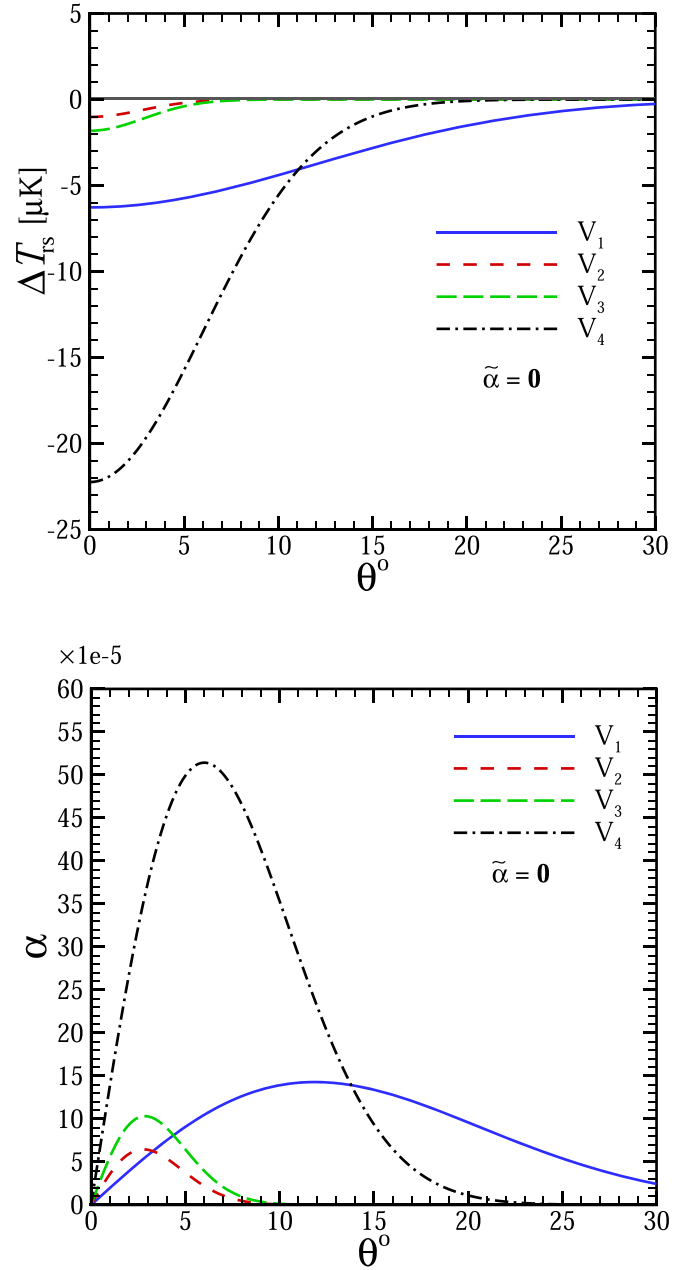


**Figure 1.** Top: the radial profiles of temperature anisotropies due to the gravitational redshift (here only ISW) of the basic  $\Lambda$ TB subvoids for  $\tilde{\alpha} = 0$  characterized by the parameters of Table 1. Bottom: the corresponding radial profiles of the lensing deflection angle.

generally, any temperature increments. Finelli et al. (2016), therefore, modified the basic  $\Lambda$ TB template to allow for the production of a hot ring. We also explore the implications of considering this new set of templates, here called modified  $\Lambda$ TB, as candidates for CS source.

The modified  $\Lambda$ TB model is constructed by introducing a new parameter  $\tilde{\alpha}$  in the potential profile,

$$\begin{aligned} \Phi(\tau, r) = & \Phi_0 \left(1 - \tilde{\alpha} \frac{r^2}{r_0^2}\right) \exp\left[-\frac{r^2}{R_V^2}\right] \\ & \times {}_2F_1\left[1, \frac{1}{3}, \frac{11}{6}, \frac{-\Omega_\Lambda}{\Omega_m(1+z)^3}\right] \end{aligned} \quad (9)$$

that leads to the extended density profile

$$\delta(r, z_V) = \delta_V g(z_V) \exp\left(-\frac{r^2}{R_V^2}\right) \times \left(1 - \frac{2 + 7\tilde{\alpha} r^2}{3 + 3\tilde{\alpha} R_V^2} + \frac{2\tilde{\alpha} r^2}{3 + 3\tilde{\alpha} R_V^4}\right). \quad (10)$$

The corresponding ISW and lensing potential imprints, valid for  $0 \leq \tilde{\alpha} < 2$ , are calculated to be

$$\begin{aligned} \delta T_{\text{rs}}(\theta) \approx & \frac{3\sqrt{\pi}}{22} \delta_V \frac{H(z_V)\Omega_\Lambda}{H_0(1+z_V)^4} \frac{{}_2F_1\left[2, \frac{4}{3}, \frac{17}{6}, \frac{-\Omega_\Lambda}{\Omega_m(1+z_V)^3}\right]}{{}_2F_1\left[1, \frac{1}{3}, \frac{11}{6}, \frac{-\Omega_\Lambda}{\Omega_m}\right]} \\ & \times (H_0 R_V/c)^3 \left(\frac{2 - \tilde{\alpha}}{2} - \tilde{\alpha} \frac{\theta^2}{\theta_V^2}\right) \exp\left(-\frac{\theta^2}{\theta_V^2}\right) \\ & \times \left(1 + \text{erf}\left[\frac{cz_V}{H(z_V)R_V}\right]\right) \end{aligned} \quad (11)$$

(Finelli et al. 2016) and

$$\begin{aligned} \alpha(\theta) \approx & -\delta_V \frac{D_{\text{LS}} D_L}{D_S} \frac{2R_V H_0^2 \Omega_m}{c^2} \frac{{}_2F_1\left[1, \frac{1}{3}, \frac{11}{6}, \frac{-\Omega_\Lambda}{\Omega_m(1+z_V)^3}\right]}{{}_2F_1\left[1, \frac{1}{3}, \frac{11}{6}, \frac{-\Omega_\Lambda}{\Omega_m}\right]} \\ & \times \left[\tilde{\alpha} + \left(1 - \tilde{\alpha} \frac{\theta^2}{\theta_V^2}\right)\right] \theta \exp\left(-\frac{\theta^2}{\theta_V^2}\right), \end{aligned} \quad (12)$$

respectively. Obviously,  $\tilde{\alpha} = 0$  reproduces the basic  $\Lambda$ LTB profiles. For the modified templates we take  $\tilde{\alpha} = 1$ . As the void parameters, we use the estimations of Table 1. It should be noted that these parameters are specifically fitted for the basic  $\Lambda$ LTB density profiles. However, the change in  $\tilde{\alpha}$  does not drastically alter the overall density profiles, and therefore we assume the same set of parameters could be used as a first acceptable approximation to the modified  $\Lambda$ LTB model. Figure 2 illustrates the induced radial profiles of the imprints. It is interesting to note the sensitivity of the induced anisotropies to relatively small changes in the density profiles. The suggested profiles are compensated for all values of  $\tilde{\alpha}$ , with different  $\tilde{\alpha}$ s setting how quickly this compensation happens. We therefore follow a parallel approach by exploring sharply compensated subvoids, called the top-hat model, as an extreme scenario. These models have the potential of hot ring production and are introduced in the next section.

### 2.1.2. Top-hat Subvoids

Inoue & Silk (2006, 2007) proposed that the observed CMB CS can be produced by a single huge compensated void. In particular, they showed that a sharply compensated spherically symmetric void (i.e., one surrounded by a thin shell of matter that contains all the matter supposed to be in the void) can explain the CS in the microwave sky. As already discussed, their suggested void parameters were later ruled out by observations. Here we investigate the possibility that multiple shallow subvoids with this assumed template placed at lower redshifts could source the observed CS anomaly.

Martínez-González et al. (1990) and Martínez-González & Sanz (1990) used approximations to Einstein field equations for the

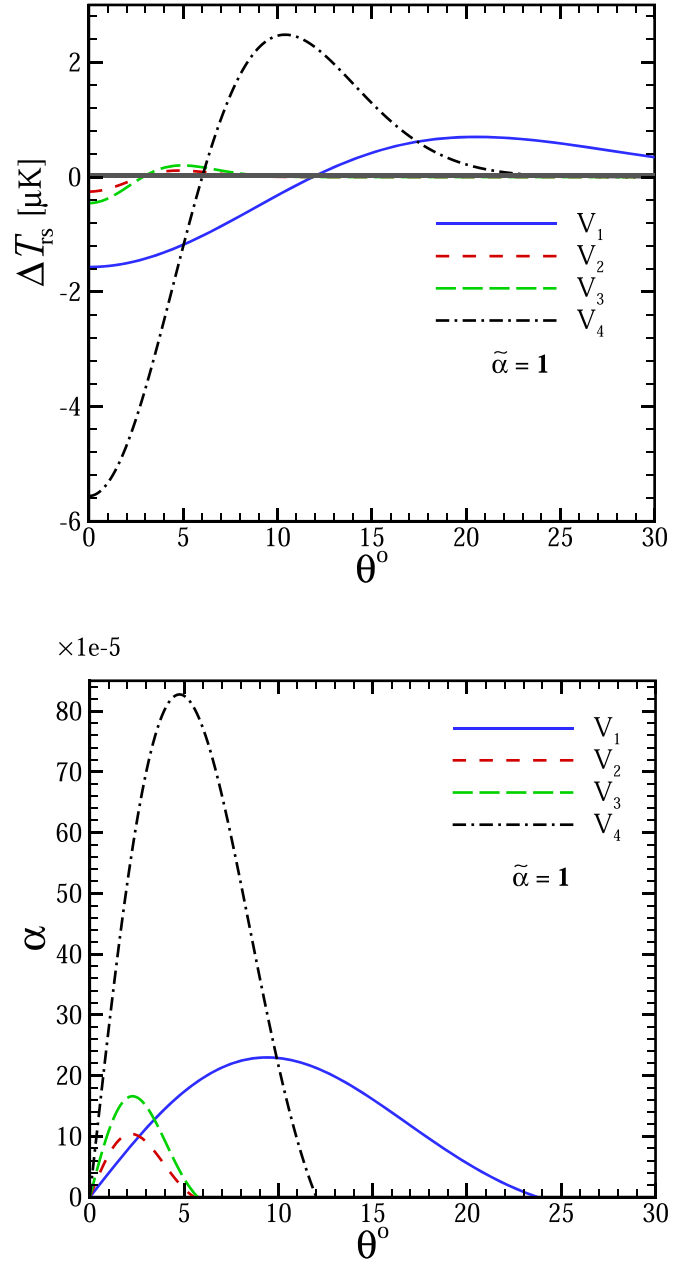


Figure 2. Similar to Figure 1 but for modified  $\Lambda$ LTB subvoids with  $\tilde{\alpha} = 1$ .

linear nonstatic potential generated by nonlinear density fluctuations to study the propagation of light and derive relatively simple expressions for the induced anisotropies in the CMB sky. Assuming a compensated spherical void as the structure with density contrast  $\delta_V$  placed at redshift  $z_V$ , with a length scale much smaller than the Hubble radius  $D_H$ , they found the following approximation for the generated anisotropy by the gravitational redshift of photons,<sup>1</sup>

$$\begin{aligned} \delta T_{\text{rs}}(\theta) \approx & -\delta_V \frac{16}{3} \left(\frac{\theta_V}{1 - d \cos \theta}\right)^3 \\ & \times \sqrt{1 - \frac{d^2 \sin^2 \theta}{\theta_V^2}} \left(\frac{9}{2}\gamma - 4 + \frac{d^2 \sin^2 \theta}{\theta_V^2}\right). \end{aligned} \quad (13)$$

<sup>1</sup> The result in Martínez-González & Sanz (1990) is for an Einstein-de Sitter universe. We follow Cruz et al. (2008) to extend to the  $\Lambda$ CDM universe with straightforward replacements.

Here  $\theta_V \propto t^\gamma$  is the angular size of the void corresponding to the comoving void radius  $R_V$ , where  $\gamma \equiv E(z) \int_z^\infty (1+z')^{-1} E(z')^{-1} dz'$  describes the propagation of the shell and  $E(z) \equiv H(z)/H_0$ . The parameter  $d$  represents the comoving distance of the observer to the center of the shell in units where  $3t_0 = 1$  and  $t_0$  is the age of the universe. Also,  $\theta$  represents the angular distance between the direction of the observation and the center of the structure. Note that Equation (13) is valid only for  $\theta \leq \sin^{-1}(\theta_V/d)$ . Above this scale the net effect of the compensated void vanishes.

With the above assumptions for the void, the deflection angle is shown to be well approximated by Martínez-González & Sanz (1990)

$$\alpha(\theta) \approx -8\delta_V \theta_V d \sin \theta \sqrt{1 - \frac{d^2 \sin^2 \theta}{\theta_V^2}}. \quad (14)$$

In this work we assume the same characterizations for the top-hat subvoids as the  $\Lambda$ LTB ones, presented in Table 1. It should be noted that these void specifications are derived through a fitting procedure of the galaxy distribution to the density profiles of the basic  $\Lambda$ LTB voids, modeled by Equation (4). However, it is easy to see that the  $\Lambda$ LTB density profiles can be sharply approximated by top-hats in their underdense regions. We therefore do not expect significant shifts in the measurements of void specifications for the top-hat profiles compared to the  $\Lambda$ LTB ones. The radial profiles for the gravitational redshift of CMB photons induced by these structures are illustrated in the upper panel of Figure 4, and their lensing deflection angles in the lower panel. It is interesting to note that the compensated top-hat profiles can produce hot spots ( $\tilde{V}_1$ ) and rings ( $\tilde{V}_2$ – $\tilde{V}_4$ ), depending on the void redshift and size. See Equation (13).

## 2.2. Collapsing Cosmic Texture

Among the proposed explanations for the observed CMB CS is a collapsing cosmic texture (Cruz et al. 2007, 2008). Cosmic textures are a type of topological defect possibly formed in phase transitions at early times, associated with symmetry breaking of certain models of high-energy physics. As the universe cools, the scalar fields present in the Higgs mechanism responsible for the symmetry breaking acquire new nonzero expectation values and therefore form a vacuum manifold with a nontrivial topology. This can be achieved, e.g., when a global  $\mathcal{O}(N)$  symmetry is broken spontaneously by  $N$  scalar fields. In this case, for  $N = 4$  the corresponding vacuum manifold is a three-sphere and the defects are called textures (Mukhanov 2005).

Textures are unstable and, after formation, textures first undergo collapse due to causal contact with their surroundings, and subsequently unwind when the gradient of the field energy surpasses the energy necessary to restore the global symmetry and emit outgoing massless radiation (Turok 1989; Turok & Spergel 1990; Vilenkin & Shellard 2000). The photons passing through the nonstatic gravitational potential of a collapsing (expanding) texture would experience gravitational redshift (blueshift) and therefore a decrease (an increase) in their temperature. Such temperature anisotropies are approximated

by Pen et al. (1994)

$$\delta T_{\text{rs}}(\theta) = -\epsilon \frac{1}{\sqrt{1 + 4\frac{\theta^2}{\theta_T^2}}} \theta \leq \theta_*. \quad (15)$$

Here  $\theta$  represents the angular separation of the direction of the observation from the CS center as before and  $\theta_* \equiv \sqrt{3}/2\theta_T$ , where  $\theta_T$  is the characteristic angular size of the texture. We have used the minus sign on the right-hand side since to have a cold spot redshifted (and not blueshifted) photons are required. The  $\epsilon$  is associated with the energy scale,  $\psi_0$ , of the symmetry breaking phase transition through  $\epsilon = 8\pi^2 G \psi_0^2$ . The radius  $\theta_T$  is determined by the dynamics of the universe, as well as the redshift of the texture  $z_T$ , through

$$\theta_T = \frac{2\sqrt{2}\kappa(1+z_T)}{E(z_T) \int_0^{z_T} dz/E(z)}, \quad (16)$$

where  $\kappa$  is a fraction of unity set from simulations. It should be noted that the approximate profile of Equation (15) is only valid for temperature anisotropies up to  $\theta \approx \theta_T$ . It can be extended to larger separations assuming the continuity of the profile and its first derivative at  $\theta_T$ . In this work we follow Vielva (2010) and use the following smooth extension for the template,

$$\delta T_{\text{rs}}(\theta) = -\frac{\epsilon}{2} e^{-(\theta^2 - \theta_*^2)/2\theta_T^2}. \quad (17)$$

In addition to generating anisotropies in the microwave sky by gravitational redshift, the texture potential also acts as a converging lens and bends the trajectories of the photons passing through it. For the collapsing cosmic texture, the deflection angle is modeled as (Durrer et al. 1992; Das & Spergel 2009)

$$\alpha(\theta) = A_T \frac{\theta}{\sqrt{1 + 4\frac{\theta^2}{\theta_T^2}}}. \quad (18)$$

Here  $A_T \equiv \frac{2\sqrt{2}\epsilon D_{\text{LS}}}{\theta_T D_S}$ , with  $D_S$  and  $D_{\text{LS}}$  representing the comoving distances of the source to the observer and to the lens, respectively. We follow the template fitting of earlier works based on WMAP data (Cruz et al. 2007) to adopt  $\epsilon = 4 \times 10^{-5}$  and  $\theta_T \approx 5^\circ$ . This places the texture at redshift  $z_T \sim 6$  and gives  $A_T \approx 4.45 \times 10^{-4}$ . The upper panel of Figure 4 represents the radial profile of the redshift-induced anisotropies, while the lower panel shows the deflection angle due to the collapsing cosmic texture discussed above.

## 3. Analysis

In the previous section we discussed the theoretical framework for the contribution to CMB anisotropies from the gravitational effects of multiple subvoids and a collapsing cosmic texture. We now explain our analysis method with the aim to investigate the detectability (and consistency) of the traces of these structures by the Planck temperature data. The data sets consist of disks with radii  $R = 10^\circ$  and  $R = 20^\circ$ , centered at the center of the CS, cut from the Planck SMICA temperature map<sup>2</sup>

<sup>2</sup> <https://pla.esac.esa.int/#home>

(Planck Collaboration et al. 2020b). The results presented here are with the HEALPix<sup>3</sup> resolution characterized by  $N_{\text{side}} = 256$  for  $R = 10^\circ$  and  $N_{\text{side}} = 128$  for  $R = 20^\circ$ , corresponding to pixel sizes of  $\approx 14'$  and  $\approx 28'$  respectively.

We first consider the case for a single structure (either the sum of the imprints of multiple subvoids or a cosmic texture). For a joint analysis of its gravitational redshift and lensing traces, assume that the observed temperature anisotropy of the patch can be modeled as

$$\delta T_{\text{obs}} = \delta T_{\text{pri}} + \mathcal{A}_{\text{rs}} \delta T_{\text{rs}} + \mathcal{A}_{\text{ln}} \delta T_{\text{ln}} + n, \quad (19)$$

where  $\delta T_{\text{obs}}$  and  $\delta T_{\text{pri}}$  represent the observed and primordial CMB anisotropies, respectively. The contribution from the instrumental noise is represented by  $n$ . The template  $\delta T_{\text{rs}}$  denotes the template of the redshifted signal produced by some decaying potential, here due to an expanding void or a collapsing texture. The  $\delta T_{\text{ln}}$  describes the fluctuations due to the lensing of CMB photons by the same source (see Equations (7)) characterized by the deflection angle  $\alpha(\theta)$  modeled by Equation (12), (14), or (18). The corresponding amplitudes for the templates,  $\mathcal{A}_{\text{rs}}$  and  $\mathcal{A}_{\text{ln}}$ , are free parameters to be simultaneously estimated from the data, and are expected to agree within the error bars if our assumed scenario of the source of the CS makes a consistent picture. Disagreements would then hint to possible inconsistencies in the ISW and lensing templates, improper parameter values fixed a priori for template construction, or may even challenge the plausibility of the model. Within this framework, the likelihood of data  $\mathcal{L}$ , given the CS parameter pair  $(\mathcal{A}_{\text{ln}}, \mathcal{A}_{\text{rs}})$ , can be expressed through

$$-2 \ln \mathcal{L}(g | \mathcal{A}_{\text{ln}}, \mathcal{A}_{\text{rs}}) = g^T \mathbf{C}^{-1} g + \text{constant}, \quad (20)$$

where  $g \equiv g(\mathcal{A}_{\text{ln}}, \mathcal{A}_{\text{rs}}) = \delta T_{\text{obs}} - [\mathcal{A}_{\text{rs}} \delta T_{\text{rs}} + \mathcal{A}_{\text{ln}} \delta T_{\text{ln}}]$  is the Gaussian signal left when the CS contribution is properly subtracted from the observed data. We have made the simplifying assumption that the background primordial signal as well as the instrumental noise can be considered Gaussian. We construct the theoretically expected pixel–pixel covariance matrix for this Gaussian part,  $\mathbf{C}_{pp'} \equiv \langle g_p g_{p'}^T \rangle$ , from the full sky (except for the mask) Planck temperature map. More specifically, we build the correlation function  $C(\rho)$ , where  $\rho$  is the angular separation of any pixel pair on the sphere, and use  $C(\rho)$  to construct the  $\mathbf{C}$  matrix for the desired patch. The best-fit values of the parameter pair  $(\mathcal{A}_{\text{rs}}^{\text{bf}}, \mathcal{A}_{\text{ln}}^{\text{bf}})$  maximize their posterior probability distribution. Assuming uniform prior on the parameters in the vicinity of this best-fit point, the pair  $(\mathcal{A}_{\text{rs}}^{\text{bf}}, \mathcal{A}_{\text{ln}}^{\text{bf}})$  would also maximize the likelihood

$$\left. \frac{\partial \mathcal{L}}{\partial \mathcal{A}_{\text{rs}}} \right|_{\text{bf}} = 0, \quad \left. \frac{\partial \mathcal{L}}{\partial \mathcal{A}_{\text{ln}}} \right|_{\text{bf}} = 0 \quad (21)$$

yielding

$$\begin{aligned} \mathcal{A}_{\text{rs}}^{\text{bf}} &= \beta [(\delta T_{\text{ln}}^\dagger \mathbf{C}^{-1} \delta T_{\text{ln}})(\delta T_{\text{rs}}^\dagger \mathbf{C}^{-1} \delta T_{\text{obs}}) \\ &\quad - (\delta T_{\text{rs}}^\dagger \mathbf{C}^{-1} \delta T_{\text{ln}})(\delta T_{\text{ln}}^\dagger \mathbf{C}^{-1} \delta T_{\text{obs}})] \\ \mathcal{A}_{\text{ln}}^{\text{bf}} &= \beta [(\delta T_{\text{rs}}^\dagger \mathbf{C}^{-1} \delta T_{\text{rs}})(\delta T_{\text{ln}}^\dagger \mathbf{C}^{-1} \delta T_{\text{obs}}) \\ &\quad - (\delta T_{\text{ln}}^\dagger \mathbf{C}^{-1} \delta T_{\text{rs}})(\delta T_{\text{rs}}^\dagger \mathbf{C}^{-1} \delta T_{\text{obs}})] \end{aligned} \quad (22)$$

where

$$\begin{aligned} \beta^{-1} &\equiv (\delta T_{\text{rs}}^\dagger \mathbf{C}^{-1} \delta T_{\text{rs}})(\delta T_{\text{ln}}^\dagger \mathbf{C}^{-1} \delta T_{\text{ln}}) \\ &\quad - (\delta T_{\text{rs}}^\dagger \mathbf{C}^{-1} \delta T_{\text{ln}})(\delta T_{\text{ln}}^\dagger \mathbf{C}^{-1} \delta T_{\text{rs}}). \end{aligned} \quad (23)$$

One could use the width of the likelihood surface, i.e., the square root of the diagonals of the Fisher inverse, to get an estimate of the measurement error,

$$\sigma_{\text{rs}}^2 = \left. \frac{\partial^2 \mathcal{L}}{\partial \mathcal{A}_{\text{rs}}^2} \right|_{\text{bf}}, \quad \sigma_{\text{ln}}^2 = \left. \frac{\partial^2 \mathcal{L}}{\partial \mathcal{A}_{\text{ln}}^2} \right|_{\text{bf}}. \quad (24)$$

They yield reliable estimates of the uncertainties for close-to-Gaussian distributions, and a lower limit otherwise. Using Equation (20) we get

$$\begin{aligned} \sigma_{\text{rs}} &= \sqrt{(\delta T_{\text{ln}}^\dagger \mathbf{C}^{-1} \delta T_{\text{ln}}) / \beta}, \\ \sigma_{\text{ln}} &= \sqrt{(\delta T_{\text{rs}}^\dagger \mathbf{C}^{-1} \delta T_{\text{rs}}) / \beta}. \end{aligned} \quad (25)$$

In the next section we also consider cases where the amplitudes of the individual subvoids are considered as free parameters and their consistency with the suggested values of Table 1 is investigated. The extension of the above framework to these cases with several varying amplitudes is straightforward,

$$\delta T_{\text{obs}} = \delta T_{\text{pri}} + \mathcal{A}_{\text{rs}} \cdot \delta T_{\text{rs}} + \mathcal{A}_{\text{ln}} \cdot \delta T_{\text{ln}} + n, \quad (26)$$

where  $\delta T_{\text{rs}}$  and  $\delta T_{\text{ln}}$  are the arrays of the gravitational redshift and lensing templates and  $\mathcal{A}_{\text{rs}}$  and  $\mathcal{A}_{\text{ln}}$  are the arrays of their amplitudes. We see in the next section that the correlation between lensing and redshifted signal is tiny. We therefore neglect it here. The best-fit amplitudes and their Fisher-based errors can be found similar to the previous case of a single structure, and we get

$$\mathcal{A}_{\diamond}^{\text{bf}} = M_{\diamond}^{-1} \cdot \mathbf{d}_{\diamond}, \quad \sigma_{\diamond} = \text{diag}(M_{\diamond}^{-1}), \quad (27)$$

where

$$\mathbf{d}_{\diamond} = \delta T_{\diamond} \mathbf{C}^{-1} \delta T_{\text{obs}}, \quad M_{\diamond} = \delta T_{\diamond} \mathbf{C}^{-1} \delta T_{\diamond} \quad (28)$$

and the symbol  $\diamond$  represents either rs or ln. Equation (27) reduces to Equations (22) and (25) for the case of a texture or a single void.

## 4. Results

We follow the method explained in the previous section to measure the amplitudes of the gravitational redshift and lensing templates for the candidates introduced in Section 2. We calculate the Fisher-estimated errors for  $\mathcal{A}_{\text{rs}}$  and  $\mathcal{A}_{\text{ln}}$  with all other standard parameters fixed. As stated in the 1, an important feature of the observed cold spot in CMB maps is the hot ring, with  $R \approx 15^\circ$ , surrounding the inner cold region. Therefore, a realistic explanation of the CS requires capturing this ring as well. We explore how extending the patch radius to  $R = 20^\circ$ , including the ring, would affect the results. For these larger disks, we reduce the resolution to  $N_{\text{side}} = 128$  to reduce the computational cost.

Table 2 presents the measured amplitudes of the sum of the subvoid templates of Figures 1–3, corresponding to  $\sum V_i(\tilde{\alpha} = 0)$ ,  $\sum V_i(\tilde{\alpha} = 1)$  and  $\sum \tilde{V}_i$ , respectively, as well as the texture of Figure 4, for patches with  $R = 10^\circ$  and  $R = 20^\circ$  centered at the CS. The amplitudes for the gravitational redshift

<sup>3</sup> <https://healpix.sourceforge.io>

**Table 2**

The Amplitudes of the Gravitational Redshift  $\mathcal{A}_{rs}$  and the Lensing Amplitude  $\mathcal{A}_{lens}$  for the Sum of the Multiple Subvoids of Table 1, Simultaneously Measured by the Planck SMICA Temperature Map (Planck Collaboration et al. 2020b)

		$\sum V_i(\tilde{\alpha} = 0)$	$\sum V_i(\tilde{\alpha} = 1)$	$\sum \tilde{V}_i$	Texture
$\mathcal{A}_{rs}$	$R = 10^\circ$	$3.4 \pm 1.5$	$16.4 \pm 3.9$	$0.1 \pm 0.1$	$1.5 \pm 0.5$
	$R = 20^\circ$	$5.4 \pm 1.4$	$14.4 \pm 3.8$	$0.3 \pm 0.1$	$1.9 \pm 0.5$
$\mathcal{A}_{ln}$	$R = 10^\circ$	$<0.1$	$<0.1$	$<0.02$	$<1.7$
	$R = 20^\circ$	$<0.2$	$<0.1$	$<0.1$	$<6.2$

**Note.** The three sets of subvoids,  $V(\tilde{\alpha} = 0)$ ,  $V(\tilde{\alpha} = 1)$ , and  $\tilde{V}$  correspond to the models of Sections 2.1.1 and 2.1.2.

are measured to be nonzero with different levels of significance, depending on the patch size, for void and the texture templates. The radial profiles of the predicted imprints for different sets of candidates are shown in Figure 5 and compared with the measured Planck profile for patches with  $R = 20^\circ$ . It is worth noting that the model parameters, and the resulting best-fit profiles, are estimated by maximizing the likelihood of Equation (20) with the full pixel covariance matrix taken into account. For the  $R = 20^\circ$  patches, the negative correlations of large pixel-pair separations can impact the results in a nontrivial way. We verified this effect by ignoring the correlations and limiting the likelihood to the diagonal terms, which is often used for a quick estimation of the amplitude, or in visual comparisons with the data profile. We noticed small changes in the measured amplitudes, depending on the patch size and template. We therefore emphasize that the measurements of Table 2 are the reliable results with the full information of the CMB temperature anisotropies taken into account (under the assumption of Gaussian primordial fluctuations).

The measured amplitudes for voids are in tension, again with different levels of significance, with  $\mathcal{A}_{rs} = 1$ , which is the expected level if the assumed template is truly capable of describing the CS. The observed high amplitudes for  $\sum V_i(\tilde{\alpha} = 0)$  and  $\sum V_i(\tilde{\alpha} = 1)$  are to be expected, given the low values of anisotropies produced by these templates (see Figures 1 and 2 in the central region of the CS where an anisotropy of  $\sim 100\text{--}150 \mu\text{K}$  is required). For the  $\sum \tilde{V}_i$  amplitudes, however, simple visual inspection should be treated with care as the templates cross the  $\delta T$  axis at small angles and assigning high amplitudes to the template would lead to large positive anisotropies at small angles, which is inconsistent with data.

It should be noted that the sum of the basic  $\Lambda\text{LTB}$  voids, unlike the modified templates with  $\tilde{\alpha} = 1$ , suffers from being incapable of reproducing the observed hot ring as the individual templates all fade to zero at large radii. The sum of the top-hat voids, on the other hand, is dominated by  $\tilde{V}_1$  on large radii (Figure 3), with little contribution close to the CS center and positive contribution at larger radii. A blind and straightforward interpretation of the measured amplitudes and their deviation from unity is to assign a different underdensity for the void obtained through multiplying the measured  $\mathcal{A}_{rs}$  by the fiducial values of Table 1, if it does not exceed  $-1$ . However, given the observational support for the fiducial underdensities, assigning a different  $\delta_v$  to the voids is hard to justify. See the discussion in Section 5.

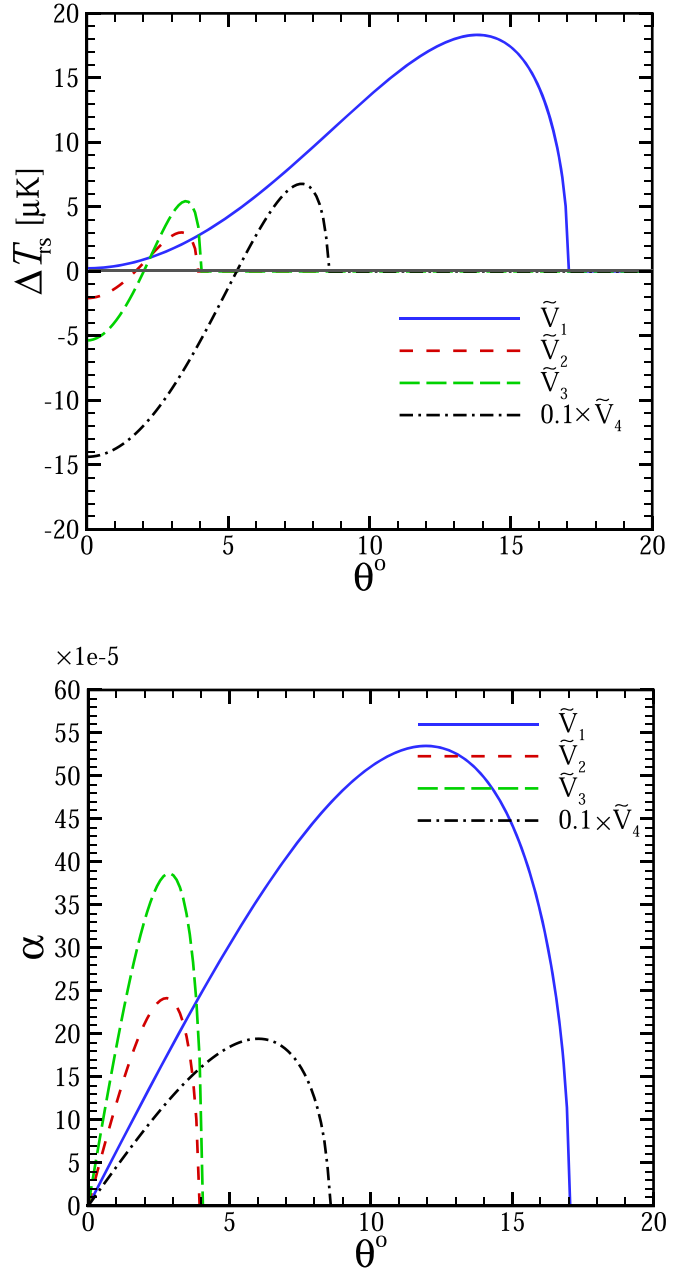


**Figure 3.** Similar to Figure 1 but for top-hat subvoids.

The measured lensing amplitudes are consistent with zero for all of these templates, and in tension with the redshifted signals of the voids. This inconsistency between the ISW and lensing amplitudes would challenge the above interpretation of the measured ISW amplitudes as a multiplier to the assumed underdensity. We also, not surprisingly, find negligible correlation between the amplitudes of the gravitational redshift and lensing templates.

The redshift imprint of texture translates to bounds on the energy scale of the corresponding phase transition through  $\epsilon = (6.0 \pm 2.0) \times 10^{-5}$  ( $1\sigma$ ) in the inner cold region and to  $\epsilon = (7.6 \pm 2.0) \times 10^{-5}$  ( $1\sigma$ ) when the outer ring is included. It should, however, be noted that the texture template smoothly goes to zero and, similar to the case of the basic  $\Lambda\text{LTB}$  subvoids, cannot reproduce the outer ring. Therefore, any

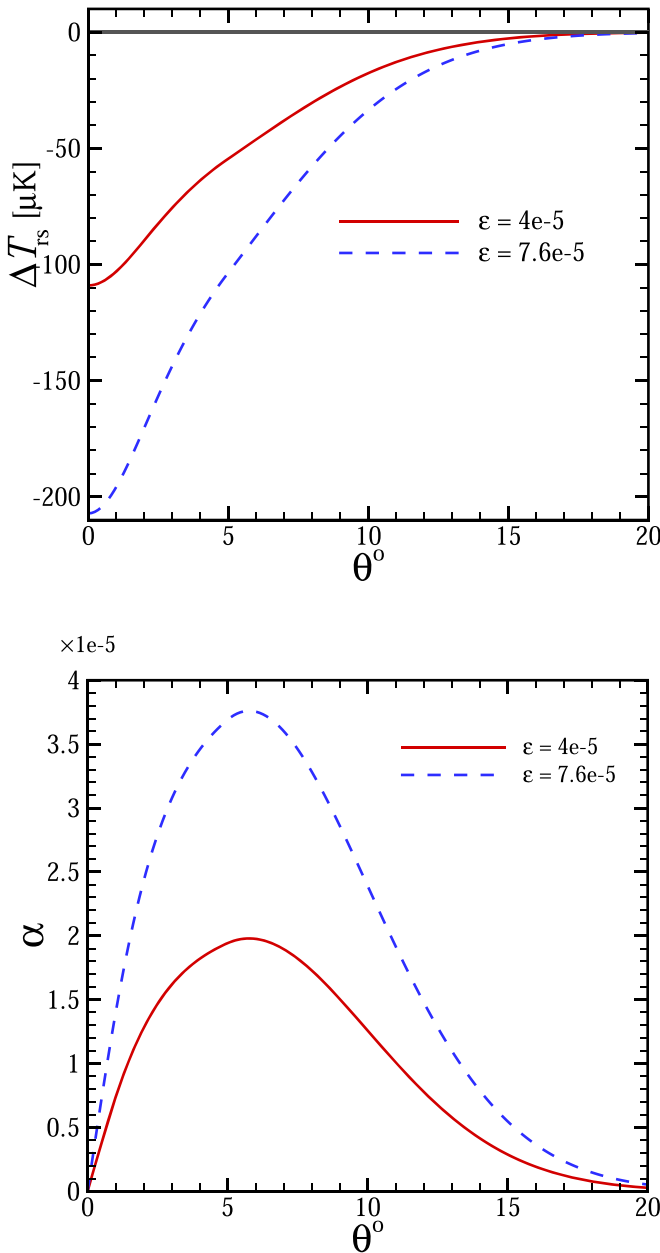


**Figure 4.** Top: the radial profiles of temperature anisotropies due to gravitational redshift of a collapsing cosmic texture. Bottom: the corresponding radial profiles of the lensing deflection angle.

conclusion about the consistency of the given texture profile with the observed CS should be taken with care.

For comparison, we also consider a case where the subvoid amplitudes are all treated as free parameters and are simultaneously measured by data, together with the corresponding lensing amplitudes. This split analysis could be regarded as a consistency check of the model to make sure not only the sum, but also the individual void profiles, when superposed, are consistent with observations. We find all the ISW amplitudes to deviate significantly and at different levels from unity and all the lensing amplitudes are measured to be consistent with zero. The results of Table 2 and these inconsistencies pose serious challenges to the interpretation of the subvoid templates as the origin of the CS in the  $\Lambda\text{CDM}$  framework.

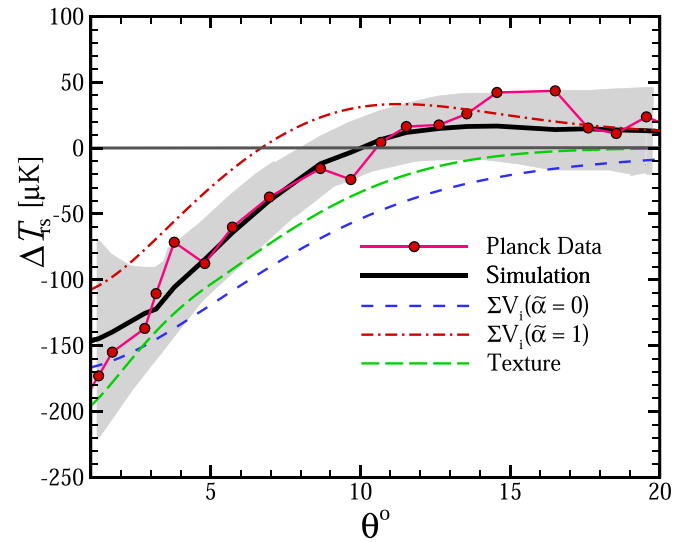


**Figure 5.** The radial profiles of the estimated gravitational redshift imprints of the multiple subvoids and texture (see Table 2). The Planck data points, the simulated profile (the solid black curve) and their corresponding error bars are taken from Figure 30 of Planck Collaboration et al. (2020c).

## 5. Summary and Discussion

In this work we addressed the possibility of the CMB cold spot being produced by the contributions of multiple subvoids or a collapsing cosmic texture. The subvoids correspond to the observations of the 2dF-VST ATLAS Cold Spot galaxy redshift survey. The goal was to search for the signatures these candidates, as physical sources of the CS, would leave on CMB temperature anisotropies, as seen by Planck, in the form of gravitational redshift and lensing parameterized by  $\mathcal{A}_{rs}$  and  $\mathcal{A}_{ln}$  respectively. In the case of nonzero amplitudes for the templates, proper comparison of the amplitudes would shed light on the self-consistency of the model. One could even consider exploiting the information in the measured amplitudes to constrain various physical parameters characterizing the candidate templates.

The nonzero amplitudes for the gravitational redshift signals of the multiple subvoids were found to deviate from unity. In the  $\Lambda\text{LTB}$  case, boosted anisotropies were required compared to the level expected from  $\Lambda\text{CDM}$ . The top-hat subvoids, on the other hand, required lower levels of anisotropies, due to being dominated by the large imprint of the fourth subvoid. The higher than expected amplitudes for the subvoid imprints were also previously claimed by other authors, e.g., see Finelli et al. (2016) and Mackenzie et al. (2017). There was also no detection for the lensing signals for any of these structures and some of the upper bounds were in significant tension with the estimated redshifted signatures.

The conclusion for the texture is somewhat different. The measured amplitude corresponds to an energy scale of  $(7.6 \pm 2.0) \times 10^{-5}$  when both the inner cold and outer hot regions are included (and lower when the hot ring is excluded). This is still below the current upper bounds on the energy scale of inflation set by the constraints on primordial gravitational waves and therefore consistent with the theoretical requirement of the symmetry breaking happening after the end of inflation (Feeney et al. 2011). However, the observed hot ring cannot be explained by the texture profile. Further conclusions about the viability of the texture hypothesis requires an explanation of

this ring as well. The upper bound on the texture lensing amplitude is consistent with one, and therefore consistent with the gravitational redshift signal and the upper bound set by inflation. Therefore, higher resolution analysis is expected to independently shed more light on the texture assumption.

We conclude that in the light of the Planck data and in the standard cosmological framework of  $\Lambda$ CDM, the various assumed subvoid templates of this work cannot reproduce the observed CS and the surrounding hot ring. The deviations of the amplitudes from unity, the tension between the gravitational redshift and lensing amplitudes, and the inconsistency of the individual void amplitudes when allowed to freely vary with the amplitude of the sum of the subvoids are serious challenges in the interpretation of the observed subvoids as the main source of the CS in the  $\Lambda$ CDM framework and call for further theoretical considerations.

One could think of modifications to the models, or exploration in a broader parameter space in a limited region allowed by the current observational bounds set by fitting the void templates with galaxy surveys. Variations in the void shape can have significant impacts on the induced temperature profiles. For example, although the underdense region of the void templates used in this work are close, the difference in the compensating overdensities that surround the inner part lead to significantly different temperature profiles. Alternative approaches include hints to primordial origins for the CS (e.g., Ringeval et al. 2016) or call for modification in the underlying cosmological model of  $\Lambda$ CDM. In particular, the size of the cold region in the top-hat voids is set by the angle where the last parenthesis in Equation (13) vanishes. This in turn is sensitive to the cosmology-dependent parameter  $\gamma$ . It is therefore expected that variations in the model of dark energy change the induced cold and hot profiles and their crossover and the resulting observational fit. If the observed 2dF-VST ATLAS subvoids are to explain the CMB CS in a different cosmological scenario, not only the total ISW and lensing amplitudes, but also the simultaneously measured amplitudes of the individual subvoids should be consistent with one.

Further observational probes such as imprints on the 21 cm signal by the gravitational redshift and lensing of these structures could be used to independently assess the viability of these candidates as sources of the cold spot.

The numerical calculations of this work were carried out on the computing cluster of the Canadian Institute for Theoretical Astrophysics (CITA), University of Toronto. The authors are also grateful to Alireza Vafaei Sadr for the help in preparing the Planck simulations required at some initial stages of this work.

## References

- Acquaviva, V., & Baccigalupi, C. 2006, *PhRvD*, **74**, 103510
- Ade, P., Aghanim, N., Arnaud, M., et al. 2016, *A&A*, **594**, A21
- Afshordi, N. 2004, *PhRvD*, **70**, 083536
- Amendola, L., Kunz, M., & Sapone, D. 2008, *JCAP*, **2008**, 013
- Beck, R., Csabai, I., Racz, G., & Szapudi, I. 2018, *MNRAS*, **479**, 3582
- Bremer, M. N., Silk, J., Davies, L. J. M., & Lehnert, M. D. 2010, *MNRAS*, **404**, 69
- Cai, Y.-C., Cole, S., Jenkins, A., & Frenk, C. S. 2010, *MNRAS*, **407**, 201
- Carbone, C., Baldi, M., Pettorino, V., & Baccigalupi, C. 2013, *JCAP*, **2013**, 004
- Colberg, J. M., Sheth, R. K., Diaferio, A., Gao, L., & Yoshida, N. 2005, *MNRAS*, **360**, 216
- Courtois, H. M., Tully, R. B., Hoffman, Y., et al. 2017, *ApJL*, **847**, L6
- Cruz, M., Cayon, L., Martınez-Gonzalez, E., Vielva, P., & Jin, J. 2007, *ApJ*, **655**, 11
- Cruz, M., Martınez-Gonzalez, E., Vielva, P., et al. 2008, *MNRAS*, **390**, 913
- Cruz, M., Martınez-Gonzalez, E., Vielva, P., & Cayon, L. 2005, *MNRAS*, **356**, 29
- Cruz, M., Tucci, M., Martınez-Gonzalez, E., & Vielva, P. 2006, *MNRAS*, **369**, 57
- Cruz, M., Turok, N., Vielva, P., Martınez-Gonzalez, E., & Hobson, M. 2007, *Sci*, **318**, 1612
- Das, S., & Spergel, D. N. 2009, *PhRvD*, **79**, 043007
- Durrer, R., Heusler, M., Jetzer, P., & Straumann, N. 1992, *NuPhB*, **368**, 527
- Feeney, S. M., Johnson, M. C., Mortlock, D. J., & Peiris, H. V. 2011, *PhRvL*, **107**, 071301
- Finelli, F., Garcıa-Bellido, J., Kovacs, A., Paci, F., & Szapudi, I. 2016, *MNRAS*, **455**, 1246
- Flender, S., Hotchkiss, S., & Nadathur, S. 2013, *JCAP*, **2013**, 013
- Garcıa-Bellido, J., Durrer, R., Fenu, E., Figueroa, D. G., & Kunz, M. 2011, *PhLB*, **695**, 26
- Garcıa-Bellido, J., & Haugboelle, T. 2008, *JCAP*, **2008**, 003
- Granett, B. R., Szapudi, I., & Neyrinck, M. C. 2010, *ApJ*, **714**, 825
- Hotchkiss, S., Nadathur, S., Gottlob, S., et al. 2014, *MNRAS*, **446**, 1321
- Hoyle, F., & Vogeley, M. S. 2004, *ApJ*, **607**, 751
- Hu, W., & White, M. 1996, *ApJ*, **471**, 30
- Inoue, K. T., & Silk, J. 2006, *ApJ*, **648**, 23
- Inoue, K. T., & Silk, J. 2007, *ApJ*, **664**, 650
- Kovacs, A. 2018, *MNRAS*, **475**, 1777
- Kovacs, A., & Garcıa-Bellido, J. 2016, *MNRAS*, **462**, 1882
- Kovacs, A., & Granett, B. R. 2015, *MNRAS*, **452**, 1295
- Kovetz, E. D., & Kamionkowski, M. 2013, *PhRvL*, **110**, 171301
- Larson, D. L., & Wandelt, B. D. 2004, *ApJL*, **613**, L85
- Liddle, A. R., & Lyth, D. H. 2000, *Cosmological Inflation and Large-scale Structure* (Cambridge: Cambridge Univ. Press)
- Mackenzie, R., Shanks, T., Bremer, M. N., et al. 2017, *MNRAS*, **470**, 2328
- Marcos-Caballero, A., Fernandez-Cobos, R., Martınez-Gonzalez, E., & Vielva, P. 2016, *MNRAS*, **460**, L15
- Martınez-Gonzalez, E., Sanz, J., & Silk, J. 1990, *ApJL*, **355**, L5
- Martınez-Gonzalez, E., & Sanz, J. L. 1990, *MNRAS*, **247**, 473
- Mostaghel, B., Moshafi, H., & Movahed, S. 2018, *MNRAS*, **481**, 1799
- Mukhanov, V. 2005, *Physical Foundations of Cosmology* (Oxford: Cambridge Univ. Press)
- Nadathur, S., Lavinto, M., Hotchkiss, S., & Rasanen, S. 2014, *PhRvD*, **90**, 103510
- Papai, P., & Szapudi, I. 2010, *ApJ*, **725**, 2078
- Papai, P., Szapudi, I., & Granett, B. R. 2011, *ApJ*, **732**, 27
- Patiri, S. G., Betancort-Rijo, J. E., Prada, F., Klypin, A., & Gottlober, S. 2006, *MNRAS*, **369**, 335
- Peebles, P. 1984, *ApJ*, **284**, 439
- Peiris, H. V. 2014, in *IAU Symp. 306, Statistical Challenges in 21st Century Cosmology*, ed. A. F. Heavens, J.-L. Starck, & A. Krone-Martins (Cambridge: Cambridge Univ. Press), 124
- Pen, U.-L., Spergel, D. N., & Turok, N. 1994, *PhRvD*, **49**, 692
- Planck Collaboration, Ade, P. A. R., Aghanim, N., et al. 2014, *A&A*, **571**, A23
- Planck Collaboration, Ade, P. A. R., Aghanim, N., et al. 2016, *A&A*, **594**, A16
- Planck Collaboration, Aghanim, N., Akrami, Y., et al. 2020a, *A&A*, **641**, A6
- Planck Collaboration, Akrami, Y., Ashdown, M., et al. 2020b, *A&A*, **641**, A4
- Planck Collaboration, Akrami, Y., Ashdown, M., et al. 2020c, *A&A*, **641**, A7
- Platen, E., van de Weygaert, R., & Jones, B. J. T. 2008, *MNRAS*, **387**, 128
- Rees, M. J., & Sciama, D. W. 1968, *Natur*, **217**, 511
- Ringeval, C., Yamauchi, D., Yokoyama, J., & Bouchet, F. R. 2016, *JCAP*, **2016**, 033
- Rudnick, L., Brown, S., & Williams, L. R. 2007, *ApJ*, **671**, 40
- Sachs, R. K., & Wolfe, A. M. 1967, *ApJ*, **147**, 73
- Schafer, B. M. 2008, *MNRAS*, **388**, 1403
- Smith, K. M., & Huterer, D. 2010, *MNRAS*, **403**, 2
- Szapudi, I., Kovacs, A., Granett, B. R., et al. 2015, *MNRAS*, **450**, 288
- Turok, N. 1989, *PhRvL*, **63**, 2625
- Turok, N., & Spergel, D. 1990, *PhRvL*, **64**, 2736
- Vielva, P. 2010, *AdAst*, **2010**, 592094
- Vielva, P., Martınez-Gonzalez, E., Barreiro, R. B., Sanz, J. L., & Cayon, L. 2004, *ApJ*, **609**, 22
- Vilenkin, A., & Shellard, E. P. S. 2000, *Cosmic Strings and Other Topological Defects* (Cambridge: Cambridge Univ. Press)
- Zhang, R., & Huterer, D. 2010, *Aph*, **33**, 69
- Zibin, J. P. 2014, arXiv:1408.4442